Thrust Actuator with Passive Restoration Force for Wide Gap Magnetic Bearings

I. Royo-Silvestre[1], J.J. Beato-López[1,2], J. C. Castellano-Aldave[3], and C. Gómez-Polo[1,2]

[1]Departamento de Ciencias, Universidad Pública de Navarra, Campus de Arrosadia, 31006, Pamplona, Spain.
[2]Institute for Advanced Materials (INAMAT), Universidad Pública de Navarra, Campus de Arrosadia, 31006, Pamplona, Spain.
[3]Jerónimo de Ayanz Center, Universidad Pública de Navarra, Pamplona, 31006, Pamplona, Spain

Abstract.- Active thrust magnetic bearings provide an axial force to balance the moving parts of machines. However, most devices produce null or unbalancing passive forces. Furthermore, reported designs usually feature very small axial and radial gaps. This paper presents a thrust actuator for wide axial gaps that produces both passive and active restoring axial forces. It features a long biconical rotor and a stator housing a single winding and two permanent magnets. Simulations are done using finite-element-analysis (FEA) and compared to magnetic circuit analysis and experimental results from a prototype with a diameter of 48 mm and 20 mm axial displacement.

Corresponding autor.-
Prof. Cristina Gómez-Polo
Departamento de Ciencias. Edificio de los Acebos.
Universidad Pública de Navarra. Campus de Arrosadia. 31006 Pamplona. Spain
Phone. +34-948169576/Fax: +34-948169565/e.mail: gpolo@unavarra.es

Keywords.- Magnetic bearing, wide gap, finite element method, thrust actuator, magnetic forces.

1.- Introduction

Electromagnetic actuators are used in many industrial applications; while linear actuators can provide high thrust bidirectional forces even for wide displacement ranges [1], magnetic bearings allow the magnetic levitation and balance of rotating machines by producing radial forces or thrust forces or both [2, 3].

Magnetic bearings can be passive (PMB), made of permanent magnets (PM), or active (AMB), comprised of windings and iron cores. PMBs produce high forces but accurate balancing is not possible due to the negligible forces generated for very small displacements and the lack of active control [4, 5]. On the other hand, AMBs are not able to produce passive force (i.e. without the application of current) but allow precise positioning at a central point using a controlled current. However, the active force (i.e. due to the current applied to the windings) is low. Hybrid magnetic bearings (HMB) add PMs to the AMB [6], enabling the increment of the force but giving rise to an unbalancing passive force in many cases [2].

Hybrid thrust magnetic bearings (HTMB) always suffer a considerable unbalancing passive radial force that appears outside the gap center, although some designs minimize it [2]. Moreover, the passive axial force is usually null or unbalancing. There is also a distinction between the conventional actuator with a large iron disk as rotor core (Fig. 1(a) [2]), which is difficult to assembly, and designs with a smaller cylindrical rotor core (Fig. 1(b) [7]) [8].

On the other side, magnetic bearings can have any size but most published designs display around 10 cm diameter with air gaps g of about 0.5-1 mm. In certain reports, large gaps are considered as g>2mm [9]. However, it should be taken into account the relative dimensions of the windings and PMs. Accordingly, a wide gap can be defined considering the gap factor g/r>0.1, being r the rotor radius [10]. Reported devices rarely generate any relevant force when scaled to wide air gaps, yet there are a few examples of designs for large gap applications such as hot-wall crystal growth apparatus, rotary anode medical X-ray tubes, spinning rotor vacuum gauges, beam choppers, turbomolecular vacuum pumps, clean pumps and washing machine drums [4, 6], [11–15].

This paper proposes a new hybrid active thrust actuator with restoring passive axial force, wide axial gap (2.5 mm) and wide displacement range (±20 mm) that features a biconical rotor, see Fig. 1(c). The design is discussed and analyzed using finite-element analysis (FEA) programs. An experimental device is built and measurements are compared to predictions.

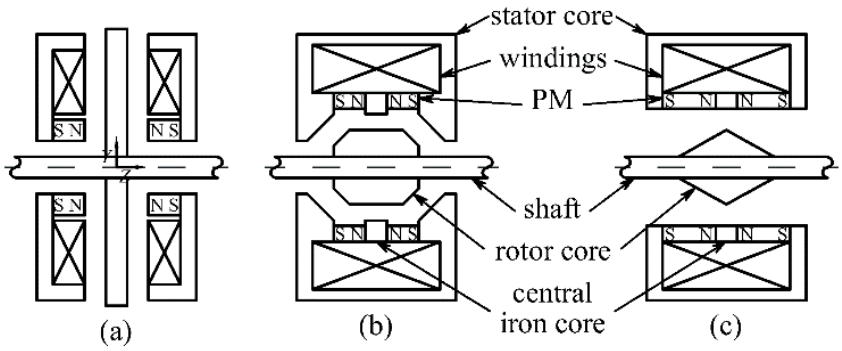

Fig. 1. Conceptual cross section of three thrust HMBs. (a) Magnetic bearing with disk rotor from [7]. (b) Actuator with tapered cylindrical rotor, detailed in [2]. (c) Proposed actuator with biconical rotor core.

2.- Design

The proposed actuator comprises a U-shaped stator and a biconical rotor as seen in Fig. 1(c) and detailed in Fig. 2. The stator iron core contains the coil winding, an iron ring, two ring-shaped PMs with axial magnetization and nonmagnetic materials between the PMs and the coil. The iron rotor is a double cone with a high length to diameter ratio, wrapped around an aluminium shaft.

As reported in [2], PMs in this type of actuator generate bias magnetic fluxes in opposite directions; when a current excites the coil a magnetic flux passes through the stator and rotor cores, decreasing the magnetic field B in one side of the rotor while increasing B in the opposite side, therefore a net force appears.

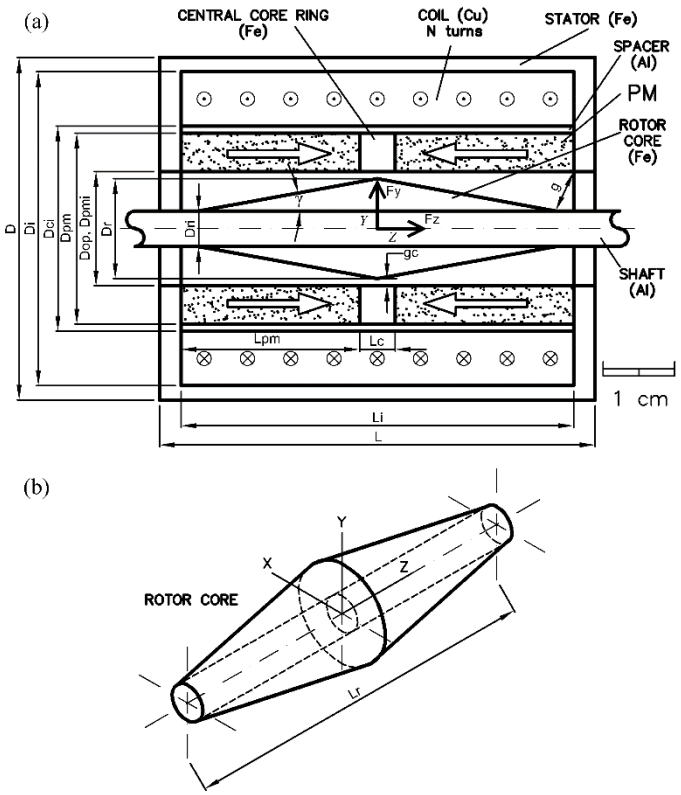

Fig. 2. Proposed actuator. (a) Sectional view. (b) Isometric detail of rotor core.

As shown in [2], forces decrease proportionally to the total gap length. However, the main differences between the previous design detailed in [2] and the proposed actuator lie in the biconical design of the rotor core. Also the lack of tapered edges eases the assembly as in [8], but there is not a defined overlap area in the proposed device. In fact, while in common actuators the main closed loop flux is the only contributor to force, in this case the disperse magnetic flux is useful due to the long biconical rotor. This represents an important achievement given that the magnetic circuit does not properly close for wide gaps.

Table I

Main parameters of the proposed device

Parameter	Value
Stator outer diameter (D)	48 mm
Stator inner diameter (D_i)	44 mm
Stator opening diameter (D_{op})	16 mm
Stator length (L)	61 mm
Stator inner length (L_i)	55 mm
Coil inner diameter (D_{ci})	28 mm
PM outer diameter (D_{pm})	26.75 mm
PM inner diameter (D_{pmi})	16 mm
PM length (L_{pm})	25 mm
Central iron core ring length (L_c)	5 mm
Rotor outer diameter (D_r)	14 mm
Rotor inner diameter (D_{ri})	5 mm
Rotor length (L_r)	50 mm
Rotor cone angle (γ)	20°
Nominal air-gap (g)	6 mm
Center radial air-gap (gc)	1 mm
Nominal axial displacement range	±20 mm
Coil turns (N)	240
Wire diameter	1 mm
Wire section	0.785 mm^2
Coil effective Cu area	188.5 mm^2
Coil packing factor	42.8 %
Dimensions	48x48x61 mm
Dimensions (with nominal rotor run)	48x48x90 mm

The parameters of the device given in Table I were constrained by the desired actuator features: a wide axial gap, small radial gap, small total diameter, simplicity, usage of easily available commercial PMs, and the demand for null or restoring passive axial force. The winding low packing factor was determined by the manufacturing quality. Note that the proposed actuator does not have a mechanical axial run limit unless auxiliary elements get added, however if the rotor moves far more than 20 mm forces are no longer adequate. The cores and rotor were made of pure iron, each PM was actually comprised of 5 stacked NdFeB grade N42 magnets, the coil was a copper winding and nonmagnetic pieces were made of aluminum. Pieces were assembled using glue or screws.

3. Analysis

3.1. Magnetic circuit

In order to analytically assess the behavior of the magnetic bearing, magnetic circuits are used. Fluxes are obtained from the magnetic circuit and forces calculated by the principle of virtual work [3]. Finally the angle of the rotor surface is taken in account [2].

A magnetic circuit based on Fig. 3(a) is solved. To simplify the thrust force (F_z) estimation, reluctances of iron and PM are neglected and PM flux is calculated as $\Phi_r=B_r \cdot S_m$ [2] (where B_r is the magnet remanence and S_m is the cross sectional xy area of the magnet). In a circuit that represents the PM as a fixed flux Φ_r, the PM reluctance R_{pm} would be parallel to Φ_r, thus R_{pm} can be neglected as long as it is much bigger than the gap reluctances [2] (that is the current case due to the large length and small cross section of both magnets). To further simplify the calculations, radial displacement is not taken into account (y=0) and air gap areas are considered constant. The right and left gaps (see

Fig. 3(a)) are approximated to $g_r \approx g\text{-}z\cdot\sin\gamma$ and $g_l \approx g+z\cdot\sin\gamma$, being g the nominal air-gap and γ the rotor cone angle (see Table I).

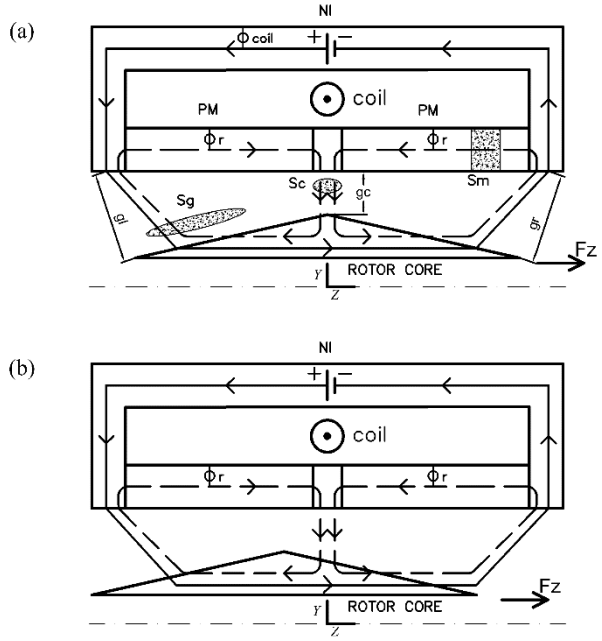

Fig. 3. Working principle of the proposed actuator, indicating the main parameters involved in the axial force estimation through magnetic circuit analysis: (a) $z = 0$ and (b) $|z| > \frac{L_c}{2}$.

Accordingly, F_z as a function of the displacement z can be expressed as:

$$\begin{cases} for -\frac{L_c}{2} < z < \frac{L_c}{2}, F_z = \left(\frac{NIB_rS_m}{g\sigma_m} + \frac{zB_r^2S_m^2\sin\gamma}{g\mu_0S_g\sigma_m^2} - \frac{4zB_r^2S_m^2}{\mu_0L_cS_c\sigma_m^2}\right)\sin\gamma \\ for\ z > \frac{L_c}{2}, F_z = \left(\frac{NIB_rS_m}{g\sigma_m} + \frac{zB_r^2S_m^2\sin\gamma}{g\mu_0S_g\sigma_m^2} - \frac{2B_r^2S_m^2}{\mu_0S_c\sigma_m^2}\right)\sin\gamma \\ for\ z < -\frac{L_c}{2}, F_z = \left(\frac{NIB_rS_m}{g\sigma_m} + \frac{zB_r^2S_m^2\sin\gamma}{g\mu_0S_g\sigma_m^2} + \frac{2B_r^2S_m^2}{\mu_0S_c\sigma_m^2}\right)\sin\gamma \end{cases} \quad (1)$$

where S_g and S_c are the effective areas of lateral (left or right) air gaps and the central air gap, respectively (see Fig. 3(a)), N the coil turns (see Table I), σ_m the PM flux leakage coeficient, and I the current flowing through the active coil. The coil leakage has been neglected ($\sigma_c = 1$).

While S_m is the constant cross section of the magnet, S_g and S_c are linked to the effective volume that stores the magnetic energy of each gap and are modified by fringing. S_c is similar to the central iron ring inner area $k_{gc}\pi D_{pmi}L_c$ where k_{gc} is a gap coefficient that accounts for fringing. However, S_g represents a complex gap and can be calculated as the estimated air gap volume divided by the gap length g.

The first two terms in Eq. 1 for $z \neq 0$ describe the usual HTMB behavior. For $z = 0$, a linear dependence of F_z versus I is found. For $z \neq 0$, a second term appears as a result of the unbalancing force caused by PMs that increases as the rotor moves. The third term, with negative sign for $z > 0$ (positive for $z < 0$), is the balancing force caused by the biconical rotor of the proposed device. Thus, the displacement of the biconical rotor for $z > 0$ gives rise to a restoring force ($\left(-\frac{4zB_r^2S_m^2}{\mu_0 L_c S_c \sigma_m^2}\right)\sin\gamma$). This additional restoring term is caused by the PM fluxes concentrated mainly on the rotor side opposite to the displacement, if $|z| > \frac{L_c}{2}$ the third term displays a constant maximum value ($\left(\frac{2B_r^2S_m^2}{\mu_0 S_c \sigma_m^2}\right)\sin\gamma$) since the whole flux concentrates on one side as shown in Fig. 3(b). It should be noted that this restoring contribution is a specific feature associated to the conical rotor shape and it does not appear in bearings with rotors with a flat central surface. As it will be qualitatively compared in next section, this simple magnetic circuit analysis is able to describe the main results obtained for the axial force through FEA estimations (see Fig. 6).

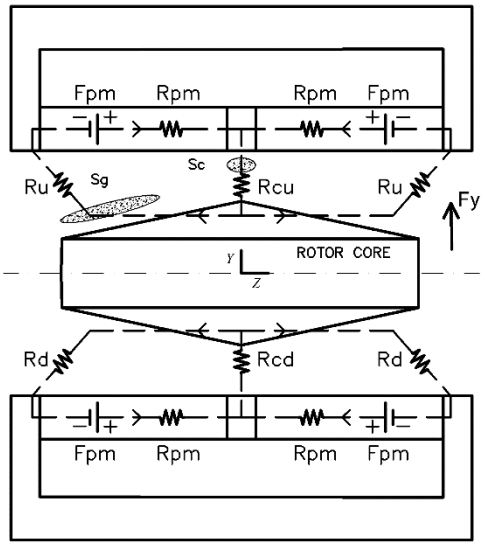

Fig. 4. Magnetic circuit used to calculate F_y for the proposed actuator ($z = 0$).

To estimate F_y a different approach is needed, PMs are modeled by a magnetomotive force F_{pm} and a reluctance R_{pm} in series [3, 7]. To simplify, iron reluctance, control current and axial displacement are ignored ($I = 0$; $z = 0$). As seen in Fig. 4 the upper and down sides are two independent circuits that only differ by the value of the reluctances. Then, the radial force F_y can be approximated by:

$$F_y = \frac{2F_{pm}^2}{\pi\sigma_m^2\mu_0 S_g}\left(\frac{4}{S_c}+\frac{2}{S_g}\right)\left(\frac{1}{(R_{pm}+R_u+2R_{cu})^2}-\frac{1}{(R_{pm}+R_d+2R_{cd})^2}\right)\cos\gamma \tag{2}$$

The magnetomotive force F_{pm} and the reluctances R can be expressed as

$$\begin{cases} F_{pm} = H_c L_{pm} \\ R_{pm} = \dfrac{L_{pm}}{\mu_0\mu_r {S_m}/_2} \\ R_u \approx \dfrac{g-y}{\mu_0 {S_g}/_2} \\ R_d \approx \dfrac{g+y}{\mu_0 {S_g}/_2} \\ R_{cu} = \dfrac{g_c-y}{\mu_0 {S_c}/_2} \\ R_{cd} = \dfrac{g_c+y}{\mu_0 {S_c}/_2} \end{cases} \tag{3}$$

where H_c, L_{pm} and μ_r are the coercitivity, length and relative permeability of the PM, respectively. Note that the actual value of effective areas S_g, S_c used for F_y calculation (Eq. 2 and Eq. 3) are the same values used for F_z calculation (Eq. 1), but $^1/_2$ factors have been applied to the areas in those equations due to the symmetries involved.

Two terms are obtained in Eq. 2, an unbalancing force ($F_y > 0$) that increases as y increases and a restoring force ($F_y < 0$) that diminishes with y. Thus, the net effect would be the increase in the F_y unbalanced force strength with the radial displacement, y. Again, this estimation basically describes the FEA results (see Fig. 9).

Although Eq. 1 and Eq. 2 model the general behavior of the proposed device, the magnetic circuit analysis is very limited in this case because fringing and leakage fluxes are important but cannot be precisely estimated. Also the effective areas S_c, S_g may vary as a function of z due to wide air gaps. For those reasons FEA analysis becomes mandatory.

3.2. FEA analysis

Two models, 2D and 3D, were solved using finite element method (FEM) software. When radial displacement $x = y = 0$ mm the problem becomes axisymmetric, the radial Forces F_x, F_y are zero and the axial Force F_z can be easily calculated as a function of the displacements z via scripting by 2D FEA freeware such as femm 4.2. When there is radial displacement the problem is solved using a commercial 3D FEA program. In both cases the Maxwell stress tensor method is applied to calculate the involved forces [5].

Fig. 5 shows the magnetic flux lines calculated by FEA for different axial positions and coil current densities J ($J=I/S$, being I the current and S the wire section). It can be seen that the working principle is subtle and hard to appreciate, as force depends

on the angle between field lines and the rotor surface, which explains why force is low for this wide axial gap. However, the higher magnetic field strength at one side of the rotor core can be noticed, to the right in Fig. 5(c) (unbalancing force), to the left in Fig. 5(d) (involving the occurrence of a restoring force on the rotor). Control flux lines are shown in absence of PMs in Fig. 5(b).

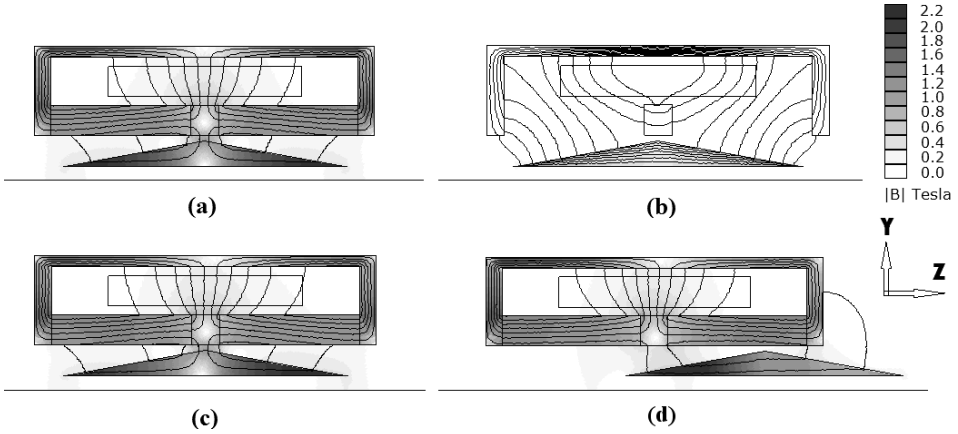

Fig. 5. 2D axysimmetric FEA simulations with flux lines and colored by the magnetic field $|B|$. (a) J = 0 A/mm^2, z = 0 mm, F_z = 0 N. (b) PMs removed, J = 4 A/mm^2, z = 0 mm, no force. (c) J = 4 A/mm^2, z = 0 mm, F_z > 0 N. (c) J = 0 A/mm^2, z = 20 mm, F_z < 0 N.

Regarding the thrust force, F_z was estimated for $x = y = 0$ at different values of the current density J. Typical values of J for this kind of devices range from 6 to 8 A/mm^2 [15]. In the present device J = 7 A/mm^2 is considered as the maximum value, that corresponds to a maximum current I = 5.5 A (similar values to those reported in [2, 8]). However, due to experimental limitations (joule heat dissipation and lack of effective refrigeration in the designed prototype) the current density was limited in the experimental prototype to 4 A/mm^2 (I = 3.1 A). Accordingly, Fig. 6 displays the estimated F_z versus displacement z. A restoring force (F_z < 0), though nonlinear with z, is always obtained under passive operation (J = 0) and for negative current densities (J = - 4 A/mm^2)

while z>0. Note that $J < 0$ would imply a magnetic field generated by the coils along the –z axis and therefore a restoring active force for $z > 0$ (opposite behavior for $J > 0$). Thus, the net force under active control ($J \neq 0$) is the result of the passive force ($J = 0$) plus the contribution of the forces associated to the current flow. This behavior is depicted in Fig. 6 for $z \leq 11$ mm, where F_z can be roughly expressed as $F_z(z) = F_z(z)_{J=0} \pm AJ$, being $F_z(z)_{J=0}$ the passive force and $A \approx 1.5$ N/A/mm^2 a constant. Accordingly, the nominal active force at $z = 0$ can be estimated equal to 6 N for $J = 4$ A/mm^2. The same value can be calculated using Eq. 1, assuming $B_r = 1.3$ T and considering a moderate leakage $\sigma_m = 1.2$.

This behavior can be well understood employing the magnetic circuit analysis (see previous section). As Eq. 1 shows, for $z = 0$ the nominal force would be given by $F_z = \left(\frac{NIB_r S_m}{g\sigma_m}\right)\sin\gamma$, while the passive force is expressed as $F_z(z)_{J=0} = \left(\frac{zB_r^2 S_m^2 \sin\gamma}{g\mu_0 S_g \sigma_m^2} - \frac{4zB_r^2 S_m^2}{\mu_0 L_c S_c \sigma_m^2}\right)\sin\gamma$. Then low active forces are caused by the wide gap g. The non-linear behavior of $F_z(z)_{J=0}$ versus z would imply a complex evolution of the effective air gaps S_c *and* S_g as the rotor moves. For $z \geq 11$ mm a more complex evolution is found, with a sharp increase in the restoring force for $J = +4$ A/mm^2. This behavior should be associated to the fact that a sizable portion of the rotor is displaced out of the stator and under these circumstances, the control flux does not overlap with the PM flux on the outward face (right side in Fig. 5(c)), while the other PM is too far to have any effect. Anyway, it can also be seen that the device is able to balance big displacements irrespectively of the current sense but with a limited ability to move the rotor to a specific uncentered point.

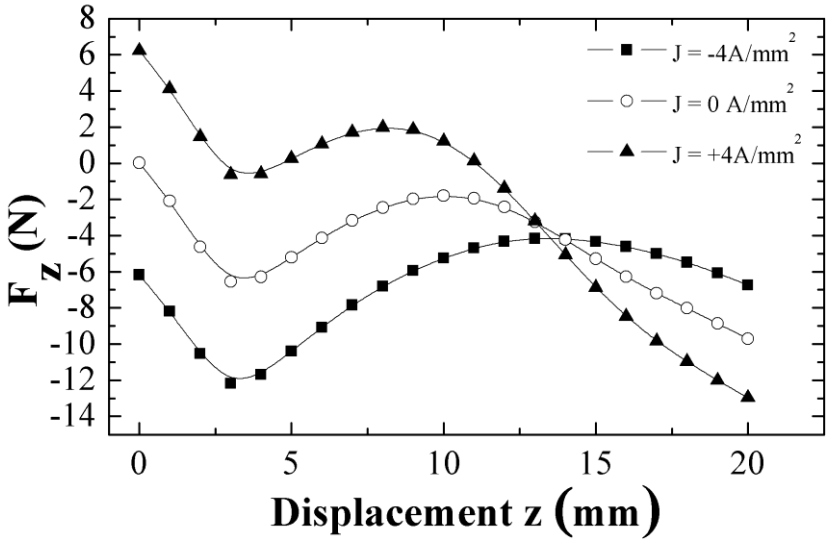

Fig. 6. Simulated axial force F_z, versus the axial displacement z, for different current densities, $x = y = 0$.

The current density dependence of F_z at different displacements (z) is depicted in Fig. 7. A linear relationship can be clearly seen as a function of z together with the occurrence of passive ($J = 0$) balancing forces when $z \neq 0$. Thus, the long biconical rotor helps to balance the axial displacements of the rotor even for $J = 0$. However, higher currents with the appropriate sign yield higher balancing forces (note that the nominal active force is 10 N when $J = 7$ A/mm^2). Again, this linear behavior can be understood in terms of Eq.1 and the magnetic circuit model. The decrease of slope of F_z vs. J for $z \neq 0$ would indicate a more complex behavior of the active force for $z > g$ (left and right gaps were approximated to $g \pm z \cdot \sin\gamma$ in order to simplify Eq. 1).

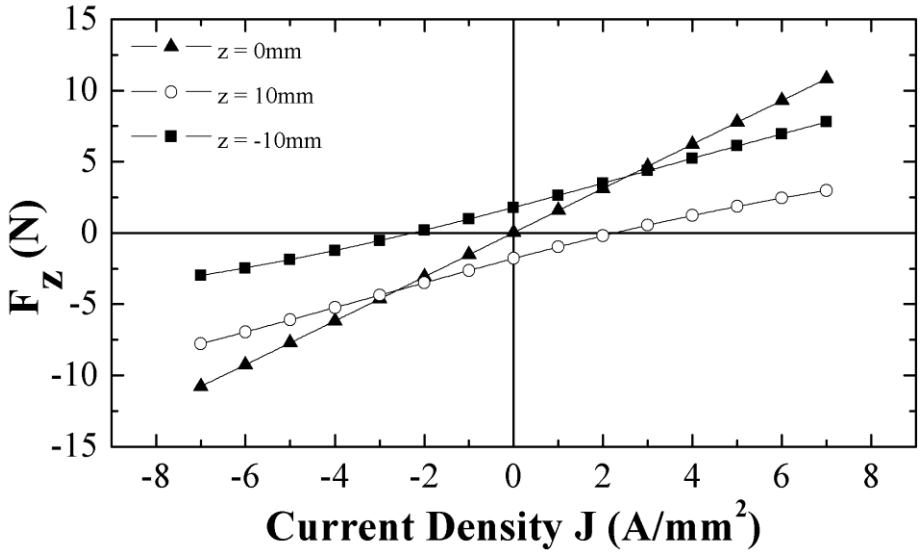

Fig. 7. Simulated excitation current density-axial force characteristics for different z displacements, $x = y = 0$.

With respect to the influence of the radial displacements y in F_z, Fig. 8 shows a negligible coupling (for a given z and J, F_z does not depend on the y displacement value) which is desirable regarding device performance.

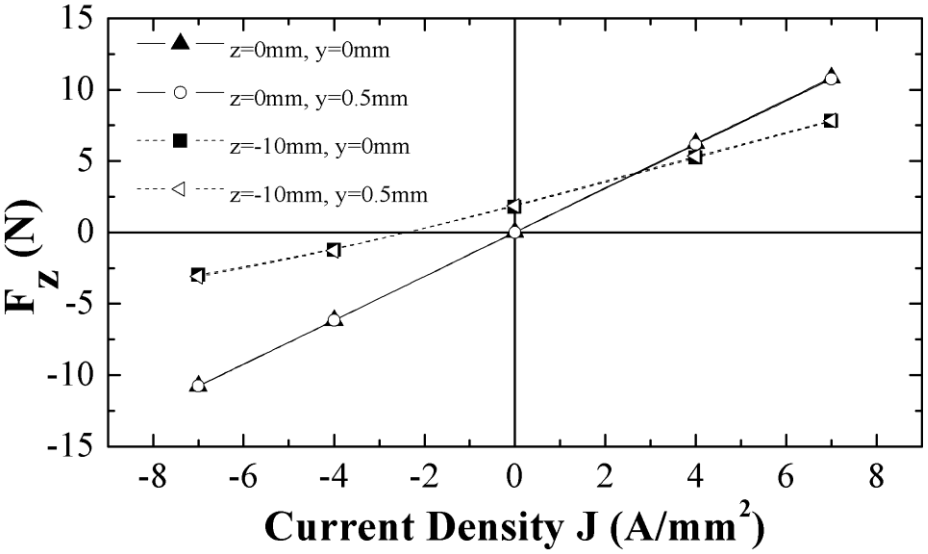

Fig. 8. Simulated F_z versus J for different radial displacements when z equals 0 and -10 mm.

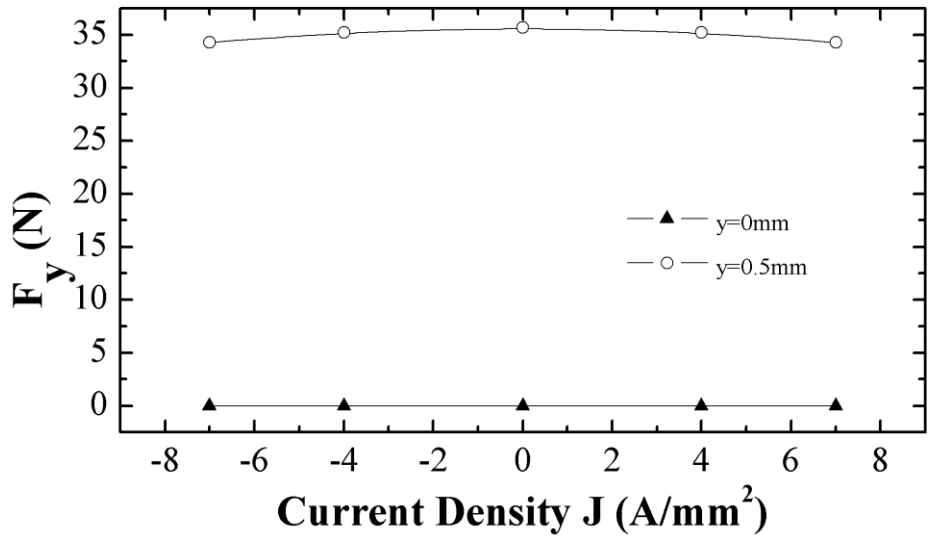

Fig. 9. Simulated *y*-direction radial force F_y versus current density, z = 0 mm.

Fig. 9 shows the radial Force F_y as a function of the coil current density. Due to the 1 mm radial gap, this unbalancing force has a significant magnitude similar to other hybrid magnetic bearings [2]. However, radial force is almost uncoupled from the windings current. Regarding the magnetic circuit model, as previously indicated the FEA estimation reproduces the general behavior obtained for z = 0 and I = 0 (see Eqs. 2 and 3); namely the increase in the F_y unbalanced force strength with the radial displacement, *y*. Also this undesired radial force decreases quickly when the rotor moves axially as seen in Fig. 10.

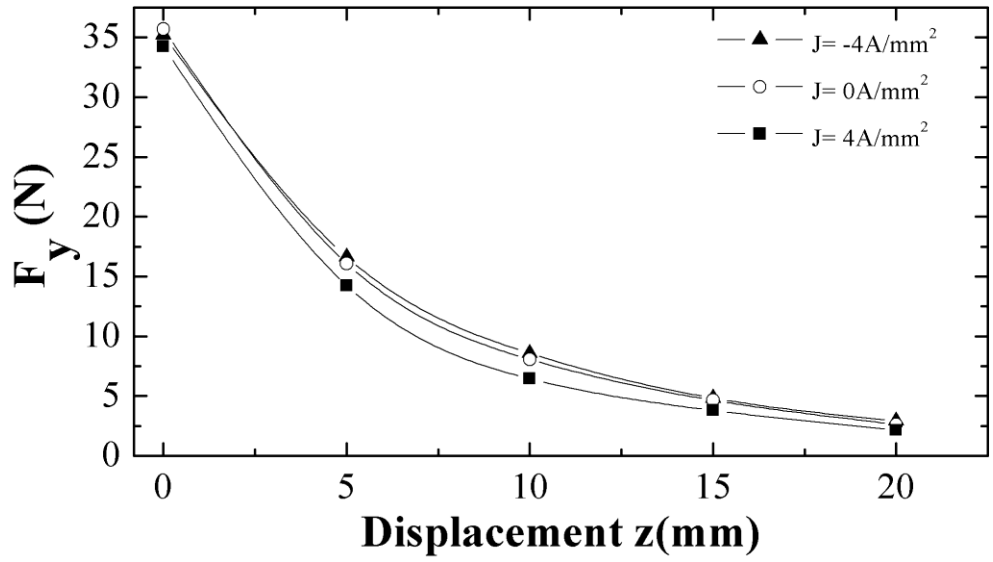

Fig. 10. Simulated radial force F_y versus displacement z when y = 0.5 mm.

For comparison, the same analysis is performed to the device described in Fig. 1(b) [2], albeit adapted to the same geometrical constraints (20 mm displacement range, 1 mm central gap, 48 mm stator diameter, keeping the taper angle as per the reference). Although that device was designed for gaps of about 1 mm, it can be scaled to moderate wider axial gaps. The characteristics of the adapted device for displacements near z = 0 mm are actually good (F_z about 5 N for J = 4 A/mm^2, almost null passive axial force and an unbalancing radial force F_y of 12 N when y = 0.5 mm). However, for higher axial displacements, radial force and coil current suffer a severe coupling, the force vs displacement curve becomes nonlinear, force severely decreases and in any case the requirement of a restoring passive axial force in all range is not met. As an example, the characteristics of the adapted design from [2] (Fig. 1(b)), compared to the device with biconical rotor proposed in this paper, are displayed in Fig. 11 for an axial displacement of -10 mm, where a restoring axial force should be positive (black dots in Fig. 11). The proposed device provides higher axial force and passive balancing axial force ($(F_z(z)_{J=0} > 0$) while the passive force of the adapted design is unbalancing ($(F_z(z)_{J=0} <$

0). Furthermore the proposed device with biconical rotor produces undesired radial unbalancing forces (white dots in Fig. 11) lower and barely coupled to current at wide displacements, in opposition to the strongly current dependent response of the adapted design.

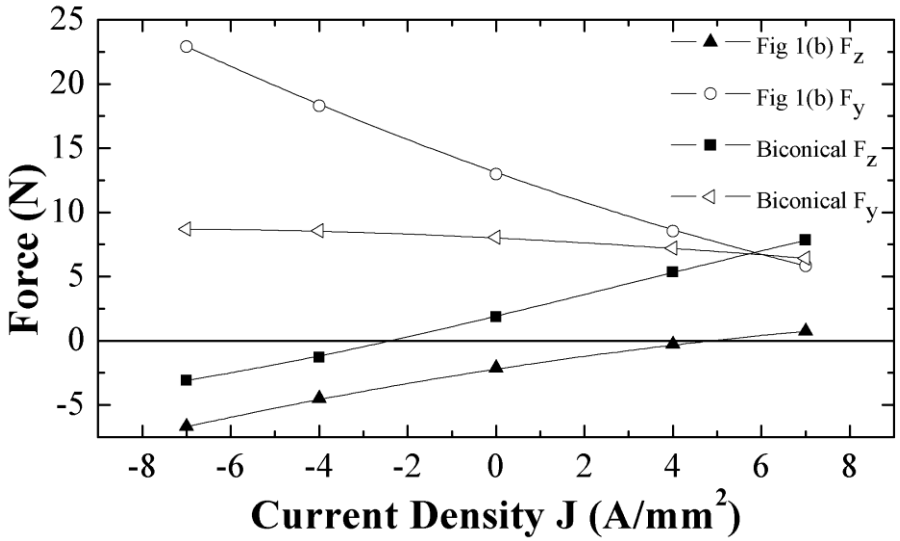

Fig. 11. Simulated forces for the adapted design from [2] compared to the proposed device with biconical rotor core, z = -10 mm, y = 0.5 mm.

4. Experimental results and discussion

A prototype was built and auxiliary nonmagnetic elements were added to restrain movement in order to properly measure the axial force as shown in Fig. 12. The windings were fed with a moderate DC control signal from a current generator, force was measured by a dynamometer. A maximum current density value J = 4 A/mm^2 was employed to avoid overheating of the coil's device.

Measured results are shown in Fig. 13. Experimental values reproduce FEA estimations; however the friction of the auxiliary elements reduces smaller forces to zero in the experiment. By manual inspection it can be seen that, in the absence of excitation, the rotor tends to self-center due to restoring axial passive forces.

It has to be noted that the device is designed to damper wide axial movements involving small forces, either as a magnetic bearing or as a linear actuator (if auxiliary elements such as bronze sleeve bushings are added) and get the rotor to a central point. Also, it can generate balancing forces even beyond z = 20 mm nominal run, but that would involve moving the rotor core out of the housing. Finally, similarly to FEA calculations a change in the trend of F_z versus z is found for high axial displacements. In fact, at z = 14 mm positive and negative coil currents swap F_z output. This behavior should ascribe, as previously outlined, to the changes in the magnetic flux contributions since the rotor is displaced out of the stator. Thus, it should be advisable to work within the nominal range of +/-14 mm with the present experimental prototype. Devices designed within less extreme constraints will also be more linear, and some improvements can be made with a better coil as 42% packing factor is rather low.

Fig. 12. Prototype. (a) Actuator with auxiliary elements to restrain the run of the rotor. (b) Dismantled actuator without auxiliary elements, the rotor core is glued to an aluminum shaft.

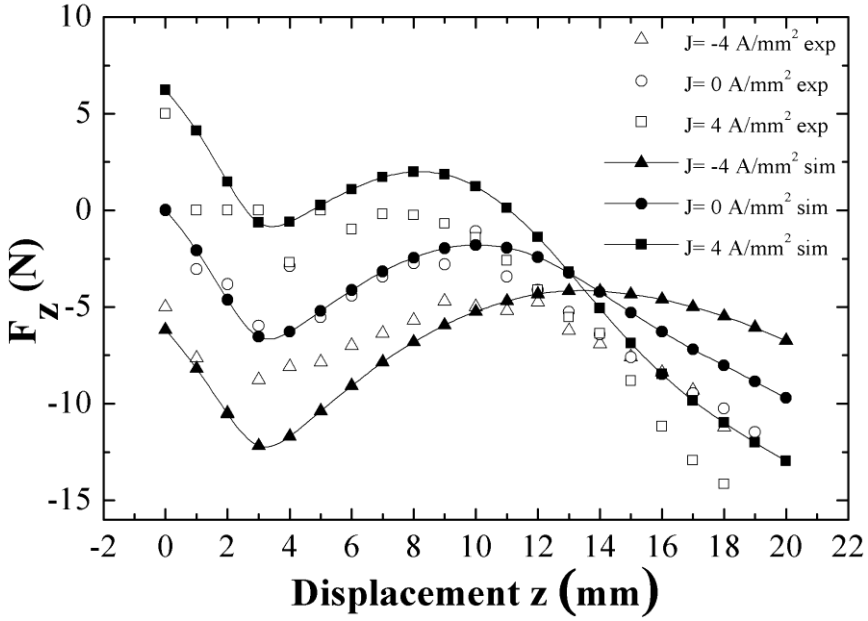

Fig. 13. Comparison of experimental and calculated results for the axial force F_z when y = 0 mm.

5. Conclusions

A wide gap hybrid thrust magnetic bearing with passive restoring axial force is presented. The actuator is composed of a biconical rotor and a U shaped stator core containing a coil, two PMs and an iron ring. The device is designed under severe size constraints and can self-center even in absence of current due its long biconical rotor iron core.

The proposed design was analyzed using a magnetic circuit and simulated by FEA, compared to an adapted existing design, and finally tested though the experimental results from a prototype. The proposed actuator shows optimum response for large displacements, has no coupling between coil current and radial force and provides a passive balancing force for displacements up to 20 mm. Simulations predict a total axial force of 6 N for current density of 4 A/mm^2 (I = 3.1 A) and 10 N for 7 A/mm^2 (I = 5.5

A). Experiments confirm its basic features, and the ability to generate at least 5 N thrust with 4 A/mm^2 coil current density.

Acknowledgements.- This work has been performed within the framework of the project BISENINT, financially supported by the Ministerio de Economia y Competitividad of Spain as part of the Programa Estatal de I+D+I Orientada a los Retos de la Sociedad under record/grant RTC-2014-2517-5.

References

[1] A. Hassan, A. Bijanzad, I. Lazoglu, Dynamic Analysis of a Novel Moving Magnet Linear Actuator, IEEE Trans. Ind. Electron. 64 (5) (2017) 3758-3766.

[2] S.-M. Yang, Y.-H. Tsai, Design of a thrust actuator for magnetic bearings with low radial attraction force, IEEE Trans. Magn. 48 (11) (2012) 3587–3590.

[3] S. Jinji, J. Ziyan, H. Weitao, L. Gang., A novel integrated 4-DOF radial hybrid magnetic bearing for MSCMG, J. Magn. Magn. Mater. 421 (2017) 86-97

[4] K. Falkowski, M. Henzel, High Efficiency Radial Passive Magnetic Bearing, Solid State Phenomena, 164 (2010) 360-365.

[5] A. Hamler, V. Goričan, B. Štumberger, M. Jesenik, M.Trlep, Passive magnetic bearing, J. Magn. Magn. Mater. 272-276 (2004) 2379-2380

[6] Y. Okada, K. Sagawa, E. Suzuki, R. Kondo, Development and Application of Parallel PM type hybrid magnetic bearings, Journal of System Design and Dynamics, 3 (4) (2009) 530-539.

[7] B. Han, S. Zheng, X. Hu, Dynamic factor models of a thrust magnetic bearing with permanent magnet bias and subsidiary air gap, IEEE Trans. Magn. 49 (3) (2013) 1221–1230.

[8] K. Hijikata, S. Kobayashi, M. Takemoto, Y. Tanaka, A. Chiba, T. Fukao, Basic characteristics of an active thrust magnetic bearing with a cylindrical rotor core, IEEE Trans. Magn. 44 (11) (2008) 4167–4170.

[9] T. Gempp, C. Redmann, R. Schöb, Active Magnetic Bearing With Large Air Gap For Operational With A 3-Phase Power Converter, in: Proceedings of the

International Gas Turbine & Aeroengine Congress & Exhibition, Indianapolis, Indiana, USA, 1999.

[10] J. Asama, M. Amada, N. Tanabe, N. Miyamoto, A. Chiba, S. Iwasaki, M. Takemoto, T. Fukao, M. A. Rahman, Evaluation of a Bearingless PM Motor With Wide Magnetic Gaps, IEEE Trans. Energy Convers. 25 (4) (2010) 957-964.

[11] Boden K., Fremery, J.K., Industrial realization of the 'System KFAJülich' permanent magnetic bearing lines, in: Proc. Of MAG'92, Alexandria, VA, USA, Jul. 1992, pp. 43-60.

[12] S. Ghiringhelli, F. Braghin, F. Castelli-Dezza, M. Carmeli, M. Mauri, M. Rossi, New large airgap Active Magnetic bearings: modeling and experimental validation, in: 2016 International Symposium on Power Electronics, Electrical Drives, Automation and Motion (SPEEDAM), Anacapri, Italy, Jun. 2016, pp. 546–551.

[13] H. Kurosu, T. Masuzawa, A. Katoh, K. Suzuki, H. Onuma, K. Kakihara; Wide gap magnetic bearing system for a magnetically suspended clean pump, in: 11th International Symposium on Magnetic Bearings, Nara, Japan, Aug. 26-29, 2008, pp. 589-593.

[14] A. V. Filatov, Generating electromagnetic forces in large air gaps, U.S. Patent 8 378 543, Feb. 19, 2013.

[15] M. Takemoto, S. Iwasaki, H. Miyazaki, A. Chiba, T. Fukao, Experimental evaluation of magnetic suspension characteristics in a 5-axis active control type bearingless motor without a thrust disk for wide-gap condition, in Proc. ECCE, Sep. 2009, pp. 2362–2367.

Figure Captions

Fig. 1. Conceptual cross section of three thrust HMBs. (a) Magnetic bearing with disk rotor from [7]. (b) Actuator with tapered cylindrical rotor, detailed in [2]. (c) Proposed actuator with biconical rotor core.

Fig. 2. Proposed actuator. (a) Sectional view. (b) Isometric detail of rotor core.

Fig. 3. Working principle of the proposed actuator, indicating the main parameters involved in the axial force estimation through magnetic circuit analysis: (a) $z = 0$ and (b) $|z| > \frac{L_c}{2}$.

Fig. 4. Magnetic circuit used to calculate F_y for the proposed actuator ($z = 0$).

Fig. 5. 2D axysimmetric FEA simulations with flux lines and colored by the magnetic field $|B|$. (a) J=0 A/mm^2, z=0 mm, F_z=0 N. (b) PMs removed, J = 4 A/mm^2, z = 0 mm, no force. (c) J = 4 A/mm^2, z=0 mm, $F_z > 0$ N. (c) J=0 A/mm^2, z= 20 mm, $F_z<0$ N.

Fig. 6. Simulated axial force F_z, versus the axial displacement z, for different current densities, x=y=0.

Fig. 7. Simulated excitation current density-axial force characteristics for different z displacements, x=y=0.

Fig. 8. Simulated F_z versus J for different radial displacements when z equals 0 and -10 mm.

Fig. 9. Simulated y-direction radial force F_y versus current density, z= 0 mm.

Fig. 10. Simulated radial force F_y versus displacement z when y= 0.5 mm.

Fig. 11. Simulated forces for the adapted design from [2] compared to the proposed device with biconical rotor core, z=-10 mm, y=0.5 mm.

Fig. 12. Prototype. (a) Actuator with auxiliary elements to restrain the run of the rotor. (b) Dismantled actuator without auxiliary elements, the rotor core is glued to an aluminium shaft.

Fig. 13. Comparison of experimental and calculated results for the axial Force F_z when y=0 mm.